Spin-orbit excitons in a correlated metal: Raman scattering study of Sr$_2$RhO$_4$

Lichen Wang,[1, *] Huimei Liu,[1, 2, †] Valentin Zimmermann,[1] Arvind Kumar Yogi,[1, 3] Masahiko Isobe,[1]
Matteo Minola,[1] Matthias Hepting,[1, ‡] Giniyat Khaliullin,[1] and Bernhard Keimer[1, §]

[1]*Max Planck Institute for Solid State Research, Heisenbergstr. 1, D-70569 Stuttgart, Germany*
[2]*Institute for Theoretical Solid State Physics and Würzburg-Dresden Cluster of Excellence ct.qmat,
IFW Dresden, Helmholtzstr. 20, 01069 Dresden, Germany*
[3]*UGC-DAE Consortium for Scientific Research (CSR), Indore Centre,
University Campus, Khandwa Road, Indore (M.P.) 452001 India*
(Dated: September 28, 2023)

Using Raman spectroscopy to study the correlated $4d$-electron metal Sr$_2$RhO$_4$, we observe pronounced excitations at 220 meV and 240 meV with A_{1g} and B_{1g} symmetries, respectively. We identify them as transitions between the spin-orbit multiplets of the Rh ions, in close analogy to the spin-orbit excitons in Mott insulators Sr$_2$IrO$_4$ and α-RuCl$_3$. This observation provides direct evidence for the unquenched spin-orbit coupling in Sr$_2$RhO$_4$. A quantitative analysis of the data reveals that the tetragonal crystal field Δ in Sr$_2$RhO$_4$ has a sign opposite to that in insulating Sr$_2$IrO$_4$, which enhances the planar xy orbital character of the effective $J = 1/2$ wavefunction. This supports a metallic ground state, and suggests that the c-axis compression of Sr$_2$RhO$_4$ may transform it into a quasi-two dimensional antiferromagnetic insulator.

Ever since the seminal work of Mott [1], correlation-driven metal-insulator transitions have been a major focal theme of solid-state research. A multitude of electronic phases – including unconventional magnetism, charge order, and superconductivity – have been identified in proximity to the Mott transition of complex materials, and increasingly elaborate models have been devised for their theoretical description [2, 3]. Spectroscopy provides some of the most powerful diagnostic abilities of the strength and influence of electronic correlations close to a metal-insulator transition, as epitomized by the single-orbital Hubbard model [4]. In its insulating state, all electrons are bound to atomic sites and can propagate incoherently via excited states with unoccupied and doubly occupied sites. In the metallic state, coherent quasiparticle bands appear at the Fermi level, but the atomic states remain visible as incoherent Hubbard bands. The intensity ratio between coherent and incoherent features in the spectral function can be used to assess the proximity to the metal-insulator transition. Experimental realizations of the single-orbital Hubbard model are rare, however, and in materials for which the Hubbard model is believed to be relevant (such as the cuprate and nickelate superconductors with one hole in the d-electron shell), the Hubbard bands tend to overlap with electronic interband transitions, thus confounding spectroscopic studies.

Recent attention has turned to correlated-electron materials with multiple active d-orbitals, which are more common and can spawn an even larger variety of electronic phases. The excitation spectra of Mott-insulating systems with multiple active d-orbitals are characterized by intra-atomic multiplets generated by the interplay of crystal-field, Hund's rule, and spin-orbit interactions; prominent examples are Mott-insulating iridates and ruthenates [5–8]. In metallic systems, the coher-

ent quasiparticles form multiple Fermi surfaces, which are subject to a complex set of instabilities as demonstrated by recent research on iron-based superconductors [9]. Due to the complex electronic structure of correlated multi-band metals, research has largely focused on the ground state and low-energy fermionic excitations near the Fermi level, whereas at least close to a metal-insulator transition, much of the spectral weight is believed to be concentrated in incoherent remnants of atomic multiplet excitations – analogues of the Hubbard bands in single-orbital compounds.

Here we report the observation of such incoherent spectral features in a carefully selected multi-orbital d-electron metal. The system we have chosen is Sr$_2$RhO$_4$, a square-planar compound with electronically active Rh ions in the $4d^5$ configuration – i.e. one hole in the t_{2g} subshell of the d-electron manifold in the nearly octahedral crystal field. Prior angle-resolved photoemission (ARPES) and quantum transport experiments have reported multiple Fermi surface sheets with sharp fermionic quasiparticles, as expected for a stoichiometric metal free of any major sources of electronic disorder [10–17]. In contrast to the more widely studied unconventional superconductor Sr$_2$RuO$_4$ (with Ru in $4d^4$ configuration) [18–20], tilt distortions of the RhO$_6$ octahedra narrow the electronic bands, thus effectively enhancing the correlation strength. Conversely, the isoelectronic compound Sr$_2$IrO$_4$ (with Ir in $5d^5$ configuration) is Mott-insulating because the larger spin-orbit coupling (SOC) of the $5d$-electrons splits the t_{2g} manifold into a pseudospin $J = 1/2$ ground state and $J = 3/2$ excited state, thus further narrowing the electronic bands [21]. Due to the single hole in the t_{2g} manifold, the intra-atomic multiplet excitations of Sr$_2$IrO$_4$ comprise a simple set of $J = 1/2 \rightarrow 3/2$ excitations (termed "spin-orbit excitons") that are optically inactive but observ-
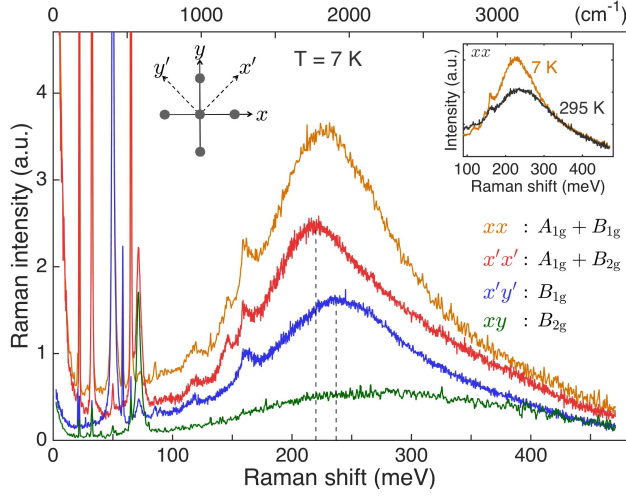
FIG. 1: Raman spectra taken with the 632.8 nm (1.96 eV) excitation line in different scattering geometries. Sharp peaks below 100 meV are phonons. The dashed lines at 220 meV and 240 meV indicate the peak positions for broad electronic scattering signals. Small peaks between 100 and 170 meV can be attributed to multi-phonons. Left inset: the light polarization directions with respect to Rh ions (black dots). Right inset: the xx spectra measured at 7 K and 295 K.

FIG. 2: Experimental spectra in A_{1g} and B_{1g} channels (grey lines) after extracting the low energy phonon peaks. The fit curves (black) include a Lorenztian tail of the elastic line (thin grey), and the spin-orbit exciton bands B (blue) and C (red). Their peak positions and intensities are calculated theoretically (see text), while the Lorenztian linewidths are adjusted to fit the experimental data.

able by Raman and resonant x-ray scattering spectroscopies [5, 6]. We have used polarization-resolved electronic Raman scattering to detect incoherent but well-defined spin-orbit exciton features in Sr_2RhO_4, and show that quantitative analysis of the Raman spectra is a rich source of information on the electronic structure of this strongly correlated metal, complementary to prior experiments on the coherent fermionic quasiparticles.

Experiment.—The high-quality single crystals of Sr_2RhO_4 were grown with the optical floating-zone technique (see Supplemental Material [22] for sample preparation and experimental details). We have collected Raman data covering the energy range up to about 500 meV with four different incident and scattered linear photon polarizations—parallel (crossed) polarizations along the nearest Rh-Rh bond denoted as xx (xy), and their counterparts after rotating by 45° denoted as $x'x'$ ($x'y'$). These scattering geometries correspond to the $A_{1g}+B_{1g}$ (B_{2g}) and $A_{1g}+B_{2g}$ (B_{1g}) representations of the D_{4h} point group [23], respectively. The observed sharp phonon peaks (Fig. 1 and [22]) are consistent with a factor-group analysis and similar to phonon spectra in the isostructural Sr_2IrO_4 [24], and are indicative of the high quality of our crystals. Whereas most of the data were taken with 632.8 nm excitation line of a He-Ne laser, the polarization dependence of the spectra was also confirmed by data collected with the 532 nm line [22].

Figure 1 shows that the Raman scattering intensity of Sr_2RhO_4 is dominated by excitations centered around 230 meV in all geometries except B_{2g}, which exhibits only a weak electronic continuum typical for metals. The
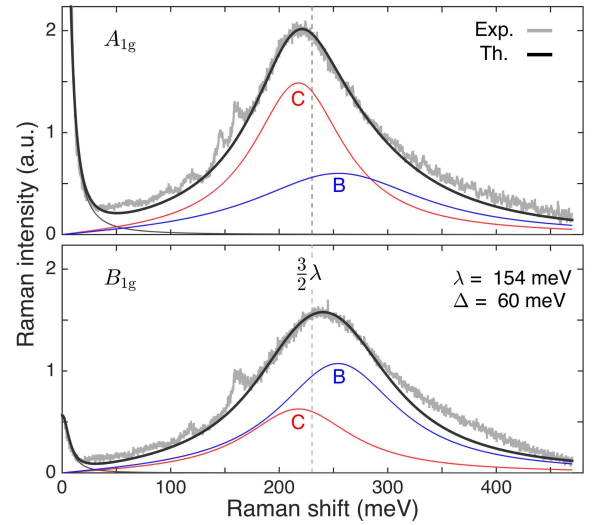
peaks are rather broad (the widths are about 150 meV at 7 K) yet well-defined even at room temperature [22]. Since the B_{2g} signal is weak, the $x'x'$ channel $A_{1g} + B_{2g}$ is dominated by the A_{1g} spectra. The xx channel comprising both A_{1g} and B_{1g} signals exhibits the strongest intensity. For the quantitative analysis of the data, we extract the pure A_{1g} spectra from the raw data in two different ways, as $xx - x'y'$ and $x'x' - xy$, which yield the nearly identical results [22]. Their average is presented in Fig. 2. The peak energies vary slightly depending on the scattering geometry. Compared to the B_{1g} symmetry, the A_{1g} signal is stronger and its peak position is lower by about 20 meV.

The spectra in Figs. 1 and 2 are highly unusual for a clean metal with well-defined quasiparticles [12], which typically only exhibit a featureless electronic continuum (as exemplified by Sr_2RuO_4 [25, 26].) A magnetic (e.g., two-magnon [23, 27]) origin of strong Raman scattering at 230 meV is unlikely, as the largest intensity is seen in the A_{1g} channel with parallel polarization. On the other hand, similar Raman features were observed in the Mott insulators Sr_2IrO_4 [5] and α-$RuCl_3$ [28, 29], and assigned to transitions between the intra-ionic $J = 1/2$ and $J = 3/2$ states [6]. These spin-orbit excitons have been found to persist also in lightly doped metallic iridates [27, 30] (although in this case, doping-induced disorder complicates the interpretation of the spectra). In Sr_2RhO_4, the energy scale of 230 meV is very similar to the spin-orbit splitting $\frac{3}{2}\lambda$ with $\lambda \sim 160$ meV (slightly reduced from a Rh^{4+} free-ion value of ~ 190 meV [31] by

covalency effects). Remarkably, spin-orbit levels in the range of $200 - 250$ meV have been predicted by quantum chemistry calculations for Sr_2RhO_4 [32]. The above considerations point towards the spin-orbit exciton origin of the observed Raman peaks. Below, we develop a theory for Raman scattering from spin-orbit excitons, which describes our data on a quantitative level.

Theory.—In an octahedral crystal field, the Rh^{4+} ion contains a single hole in the t_{2g} orbital level, hosting spin $s = 1/2$ and effective orbital $l = 1$ moments. The crystal field induced by the tetragonal distortion, $\frac{1}{3}\Delta(n_{yz} + n_{zx} - 2n_{xy}) = \Delta(l_z^2 - \frac{2}{3})$, splits this level into an xy singlet and an xz/yz doublet (Fig. 3(a)). On the other hand, the spin-orbit coupling $\lambda(\boldsymbol{l} \cdot \boldsymbol{s})$ forms multiplets with total angular momentum $J = 1/2$ and $3/2$. The combined action of these interactions results in a level structure comprising the ground state Kramers doublet A with an effective spin $1/2$, and two excited doublets B and C derived from the $J = 3/2$ quartet states with $J_z = \pm 3/2$ and $J_z = \pm 1/2$, respectively, see Fig. 3(b). Explicit forms of the corresponding spin-orbit entangled wavefunctions can be found in the Supplemental Material [22], and their spatial shapes at representative Δ/λ values are illustrated in Fig. 3(c). With respect to the ground state A level, the energies of B and C doublets read as

$$E_{\mathrm{B}} = \frac{3}{4}\lambda + \frac{1}{2}\Delta + \frac{1}{2}R, \qquad E_{\mathrm{C}} = R, \qquad (1)$$

where $R = \sqrt{\frac{9}{4}\lambda^2 + \Delta^2 - \lambda\Delta}$. For $\Delta > 0$ ($\Delta < 0$), the B level is higher (lower) than the C level, see Fig. 3(c).

The above picture assumes that the spin-orbit excitons interact with the underlying electronic continuum, so that their spectral features are broadened. We note that the features in Fig. 1 are indeed broader than the spin-orbit exciton peaks in Mott insulators [5, 28]. In the following, we focus on the polarization dependence of the exciton peak energies and intensities, leaving the lineshape effects aside. To this end, we adopt the Fleury-Loudon theory, which describes the Raman scattering intensity in terms of spin exchange operators, with proper form-factors encoding the scattering geometry [23, 33].

In the present context, the Raman light scattering involves two subsequent optical transitions of d-electrons between neighboring Rh ions, and creates a spin-orbit exciton in the final state, as illustrated in Fig. 4. As exactly the same intersite hoppings via doubly-occupied intermediate states also appear in the derivation of the spin-orbital exchange interactions between ions, the Raman scattering operator $\mathcal{R}$ can be expressed via the corresponding exchange Hamiltonian. Based on this observation [33], we can write down the Raman operators of A_{1g} and B_{1g} symmetries as $\mathcal{R}_{A_{1g}/B_{1g}} = (\mathcal{R}_x \pm \mathcal{R}_y)$, where $\mathcal{R}_\gamma$ with $\gamma \in \{x, y\}$ is the spin-orbital exchange operator acting on nearest-neighbor $\langle ij \rangle \parallel \gamma$ bonds. For the t_{2g}
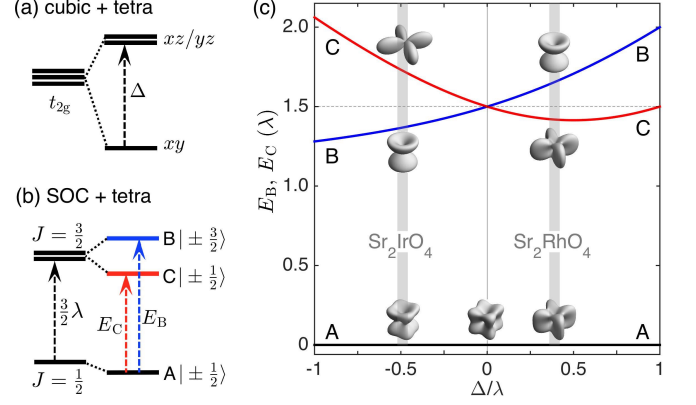

FIG. 3: Energy levels for the t_{2g} hole in tetragonal crystal field (a) without and (b) with spin-orbit coupling. In the hole language used here, $\Delta > 0$ corresponds to the oxygen octahedra with longer $z \parallel c$ axis as in Sr_2RhO_4. (c) Excitation energies E_{B} and E_{C} as a function of Δ/λ. The vertical grey stripes at $\Delta/\lambda \sim 0.4$ and $\Delta/\lambda \sim -0.5$ correspond to Sr_2RhO_4 with $\lambda \simeq 154$ meV and $\Delta \simeq 60$ meV (this work), and Sr_2IrO_4 with $\lambda \simeq 380$ meV and $\Delta \simeq -190$ meV (Ref. [6]), respectively. The spatial shapes of the t_{2g} hole wavefunctions in these two compounds are displayed; note a more flat, xy-type shape of the ground-state wavefunction in Sr_2RhO_4, in contrast to more out-of-plane xz/yz character in Sr_2IrO_4.

orbital systems with spin one-half, it has the following structure (neglecting Hund's coupling corrections) [34]:

$$\mathcal{R}_\gamma \propto \sum_{\langle ij \rangle_\gamma} \left[(4\boldsymbol{s}_i \cdot \boldsymbol{s}_j + 1)\mathcal{O}_{ij}^{(\gamma)} - l_{\gamma i}^2 - l_{\gamma j}^2 + \tau^2(l_{zi}^2 + l_{zj}^2) \right], \quad (2)$$

where the orbital operator $\mathcal{O}_{ij}^{(x)} = [(1 - l_y^2)_i(1 - l_y^2)_j + (l_y l_z)_i(l_z l_y)_j] + [y \leftrightarrow z]$, and $\mathcal{O}_{ij}^{(y)}$ follows by symmetry (replacing $y \to x$). The orbital angular momentum operators $l_x = i(d_{xy}^\dagger d_{zx} - d_{zx}^\dagger d_{xy})$, etc.

In Eq. (2), all terms but the last originate from the t_{2g}-t_{2g} orbital hoppings [34], while the τ-term stands for a contribution from nondiagonal t_{2g}-e_g hopping $\tilde{t}$. Relative to the t_{2g}-t_{2g} hopping t, it is given by $\tau \equiv \tilde{t}/t = \sin 2\alpha (t_{pd\sigma}/t_{pd\pi})$, where α quantifies the deviation of the Rh-O-Rh bond angle from the ideal $180°$, see Fig. 4(d). This contribution can be sizeable even for small α, due to the stronger σ-type overlap $t_{pd\sigma}$ between O-p and Rh-e_g orbitals, as compared to the $t_{pd\pi}$ overlap for t_{2g} states.

In general, the operator $\mathcal{R}_\gamma$ (2) creates spin, orbital, and composite spin-orbital excitations in the Raman spectra. To proceed further, we need to express this operator in terms of the A, B, and C Kramers doublet states. The mapping onto the spin-orbit basis is straightforward but lengthy, and details are provided in the Supplemental Material [22]. As a result, we obtain the Raman operators of the A_{1g} and B_{1g} symmetries, and evaluate their matrix elements corresponding to the transitions from the ground state A to the excited states B and C. Neglecting non-local spin correlations in paramagnetic Sr_2RhO_4,
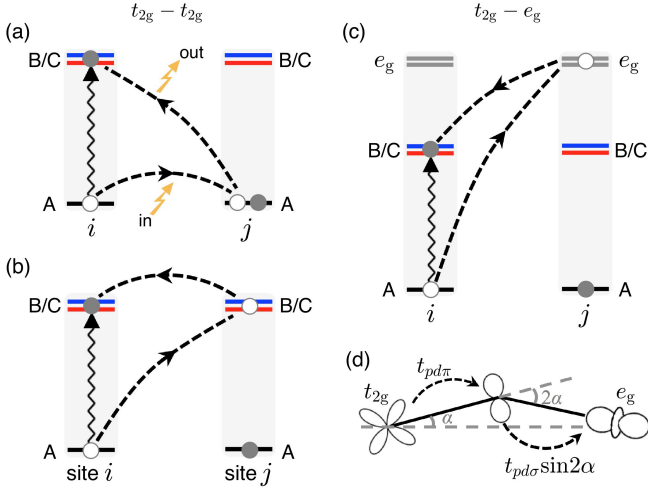
FIG. 4: Schematic of (a)-(b) t_{2g}-t_{2g} and (c) t_{2g}-e_g intersite hoppings (dashed lines) in the Raman photon-in photon-out (orange zigzag arrows) scattering process, creating spin-orbit excitations A$\to$ B/C (wavy lines) on site i. In the intermediate virtual state, site j is occupied by two holes (filled and empty circles) which experience intraionic Coulomb interaction (not shown). (d) t_{2g}-e_g hopping between d_{xy} and $d_{3x^2-r^2}$ orbitals, generated by the rotations of the oxygen octahedra around $z \parallel c$ axis by angle α. In Sr$_2$RhO$_4$, $\alpha = 10.5°$ [35].

we arrive at the following intensities of the B and C excitons in the A_{1g} scattering channel:

$$A_{1g} \begin{cases} I_B = \frac{1}{4}c_\theta^6 + \frac{1}{2}c_\theta^2(1+s_\theta^2)^2, \\ I_C = \frac{3}{4}s_\theta^2 c_\theta^2(1+s_\theta^2)^2 + s_\theta^2 c_\theta^2(c_\theta^2+4\tau^2)^2. \end{cases} \quad (3)$$

In the B_{1g} channel, we obtain:

$$B_{1g} \begin{cases} I_B = \frac{5}{4}c_\theta^6 + \frac{1}{2}c_\theta^2(1+s_\theta^2)^2, \\ I_C = \frac{3}{4}s_\theta^2 c_\theta^2(1+s_\theta^2)^2. \end{cases} \quad (4)$$

Here, $c_\theta \equiv \cos\theta$, $s_\theta \equiv \sin\theta$, and the angle $0 < \theta < \frac{\pi}{2}$ given by $\tan 2\theta = 2\sqrt{2}\lambda/(\lambda - 2\Delta)$ depends on the relative strength of the tetragonal field Δ/λ. It decides the spatial shapes of the spin-orbit wavefunctions shown in Fig. 3(c), and thus determines the intersite hopping amplitudes and Raman matrix elements. The τ-term contributes only to the A_{1g} intensity.

We note that within the present nearest-neighbor hopping model, the spin-orbit excitons do not contribute to the B_{2g} scattering. In reality, however, a small contribution $\propto (t'/t)^4$ to B_{2g} signal is expected (and possibly present in Fig. 1) due to longer-range hoppings t'.

Eqs. (1), (3), and (4) fully determine the spin-orbit exciton peak positions and intensities in the Raman spectra, as a function of three parameters: λ, Δ, and τ. We recall that τ accounts for the t_{2g}-e_g hopping, and its value is determined by the $t_{pd\sigma}/t_{pd\pi}$ ratio (for a given angle α).

Discussion.—The above theory with $\lambda = 154$ meV, $\Delta = 60$ meV, and $t_{pd\sigma}/t_{pd\pi} = 1.2$ reproduces the experimental spectra (Fig. 2) very well. The deviations

can be attributed to the particle-hole continuum, possible exciton-phonon sidebands, and multiple-excitons. Regarding the latter, we note that multiple exciton creation requires at least two subsequent intersite hoppings between the $J = 1/2$ and $J = 3/2$ levels, which are small in compounds with $180°$ exchange bonding. Therefore, the double-exciton peaks are not clearly visible in the perovskites Sr$_2$RhO$_4$ and Sr$_2$IrO$_4$. In contrast, such intersite hoppings are strong in Kitaev materials with $90°$ bonding, and pronounced double-exciton peaks have indeed been observed in α-RuCl$_3$ [28, 29].

Both B and C excitations feed into the A_{1g} and B_{1g} channels, but with unequal spectral weights (Fig. 2). The overall peak position thus depends on the scattering geometry. The A_{1g} peak is more intense than B_{1g} due to t_{2g}-e_g hopping; the opposite is expected in Ba$_2$IrO$_4$ with no octahedral rotations.

The relative order of the A_{1g} and B_{1g} peak positions uniquely determines the sign of the tetragonal field Δ, and our data firmly excludes $\Delta < 0$ values (Supplemental Material [22]). The obtained $\Delta/\lambda \simeq 0.4$ ratio is rather small, implying that all components of the orbital moment remain unquenched. While the relative strength of Δ and λ is comparable to that in Sr$_2$IrO$_4$ with $\Delta/\lambda \simeq -0.5$ [6], the signs of Δ in these compounds are opposite, despite similar lattice structures. The difference likely originates from screening of lattice Madelung potential (which gives a large negative Δ in Sr$_2$IrO$_4$ [32]) in metallic Sr$_2$RhO$_4$, so that the ligand field $\Delta > 0$ of the apically elongated (by 5% [36]) octahedra dominates. It should be interesting to include such screening effects in quantum chemistry calculations [32].

The positive (negative) Δ values increase (reduce) the planar xy orbital character of the effective $J = 1/2$ wavefunction (Fig. 3). Consequently, the in-plane effective hopping amplitude in Sr$_2$RhO$_4$ (Sr$_2$IrO$_4$) is enhanced (suppressed) from its $\Delta = 0$ value of $t_{eff} = \frac{2}{3}t$. This effect cooperates with the reduced spin-orbit coupling to support a metallic ground state in Sr$_2$RhO$_4$, and suggests that c-axis compression (changing the sign of Δ) may trigger a metal-to-insulator transition.

Our results on the spin-orbit excitons with energy ~ 230 meV are complementary to ARPES data, which mostly probe coherent fermionic quasiparticles at and near the Fermi level [10, 11, 37, 38]. Results from both probes indicate a major influence of the spin-orbit coupling on the electronic structure and dynamics. Remarkably, however, the ARPES data suggest strong orbital polarization in favor of out-of-plane xz/yz hole states, whereas the Raman data are more isotropic with preferential xy character. The coexistence of spin-orbit excitons and fermionic quasiparticles with different orbital admixtures calls for a more elaborate description of our data, for instance via a dynamical mean-field theory approach to Raman scattering [39].

In summary, using Raman spectroscopy we have ob-

served spin-orbit excitons in Sr_2RhO_4, as a direct signature of the spin-orbit entangled nature of correlated electrons in this Fermi-liquid metal. From the polarization dependence of the exciton peaks, we have quantified the spin-orbit and tetragonal crystal field parameters, which determine the orbital shapes of the corresponding wavefunctions. We found that the tetragonal field in Sr_2RhO_4 increases the planar xy orbital character of the effective $J = 1/2$ wavefunction, thereby supporting the metallic ground state. This finding calls for the x-ray absorption and light-polarized ARPES studies of the orbital character of the electronic bands in Sr_2RhO_4. Our results also suggest that flattening of the RhO_6 octahedra may drive Sr_2RhO_4 into a Mott insulating state, similar to the case of metal-insulator transition in Ca_2RuO_4 [40]. More generally, the experimental and analytical approach we have demonstrated for a disorder-free system with a relatively simple electronic structure opens up a potentially rich source of information on electronic correlations in other multi-orbital metals.

L.W. and H.L. contributed equally to this work.

————————

* lichen.wang@fkf.mpg.de
† huimei.liu@ifw-dresden.de
‡ m.hepting@fkf.mpg.de
§ b.keimer@fkf.mpg.de

[1] N. F. Mott, Rev. Mod. Phys. **40**, 677 (1968).
[2] M. Imada, A. Fujimori, and Y. Tokura, Rev. Mod. Phys. **70**, 1039 (1998).
[3] A. Georges, G. Kotliar, W. Krauth, and M. J. Rozenberg, Rev. Mod. Phys. **68**, 13 (1996).
[4] G. Kotliar and D. Vollhardt, Phys. Today **57**, 53 (2004).
[5] J.-A. Yang, Y.-P. Huang, M. Hermele, T. Qi, G. Cao, and D. Reznik, Phys. Rev. B **91**, 195140 (2015).
[6] J. Kim, M. Daghofer, A. H. Said, T. Gog, J. van den Brink, G. Khaliullin, and B. J. Kim, Nat. Commun. **5**, 4453 (2014).
[7] H. Gretarsson, H. Suzuki, H. Kim, K. Ueda, M. Krautloher, B. J. Kim, H. Yavaş, G. Khaliullin, and B. Keimer, Phys. Rev. B **100**, 045123 (2019).
[8] C. G. Fatuzzo, M. Dantz, S. Fatale, P. Olalde-Velasco, N. E. Shaik, B. Dalla Piazza, S. Toth, J. Pelliciari, R. Fittipaldi, A. Vecchione, N. Kikugawa, J. S. Brooks, H. M. Rønnow, M. Grioni, C. Rüegg, T. Schmitt, and J. Chang, Phys. Rev. B **91**, 155104 (2015).
[9] M. Yi, Y. Zhang, Z.-X. Shen, and D. Lu, npj Quantum Mater. **2**, 57 (2017).
[10] B. J. Kim, J. Yu, H. Koh, I. Nagai, S. I. Ikeda, S.-J. Oh, and C. Kim, Phys. Rev. Lett. **97**, 106401 (2006).
[11] F. Baumberger, N. J. C. Ingle, W. Meevasana, K. M. Shen, D. H. Lu, R. S. Perry, A. P. Mackenzie, Z. Hussain, D. J. Singh, and Z.-X. Shen, Phys. Rev. Lett. **96**, 246402 (2006).
[12] R. S. Perry, F. Baumberger, L. Balicas, N. Kikugawa, N. J. C. Ingle, A. Rost, J. F. Mercure, Y. Maeno, Z. X. Shen, and A. P. Mackenzie, New J. Phys. **8**, 175 (2006).
[13] M. W. Haverkort, I. S. Elfimov, L. H. Tjeng, G. A. Sawatzky, and A. Damascelli, Phys. Rev. Lett. **101**, 026406 (2008).
[14] G.-Q. Liu, V. N. Antonov, O. Jepsen, and O. K. Andersen, Phys. Rev. Lett. **101**, 026408 (2008).
[15] C. Martins, M. Aichhorn, L. Vaugier, and S. Biermann, Phys. Rev. Lett. **107**, 266404 (2011).
[16] K.-H. Ahn, K.-W. Lee, and J. Kuneš, J. Phys. Condens. Matter **27**, 085602 (2015).
[17] G. Zhang and E. Pavarini, Phys. Rev. B **99**, 125102 (2019).
[18] A. Damascelli, D. H. Lu, K. M. Shen, N. P. Armitage, F. Ronning, D. L. Feng, C. Kim, Z.-X. Shen, T. Kimura, Y. Tokura, Z. Q. Mao, and Y. Maeno, Phys. Rev. Lett. **85**, 5194 (2000).
[19] A. P. Mackenzie, S. R. Julian, A. J. Diver, G. J. McMullan, M. P. Ray, G. G. Lonzarich, Y. Maeno, S. Nishizaki, and T. Fujita, Phys. Rev. Lett. **76**, 3786 (1996).
[20] C. Bergemann, S. R. Julian, A. P. Mackenzie, S. NishiZaki, and Y. Maeno, Phys. Rev. Lett. **84**, 2662 (2000).
[21] B. J. Kim, H. Jin, S. J. Moon, J.-Y. Kim, B.-G. Park, C. S. Leem, J. Yu, T. W. Noh, C. Kim, S.-J. Oh, J.-H. Park, V. Durairaj, G. Cao, and E. Rotenberg, Phys. Rev. Lett. **101**, 076402 (2008).
[22] See Supplemental Material at *** for sample characterization, additional Raman data, and details of the theoretical analysis, which includes Ref. [41].
[23] T. P. Devereaux and R. Hackl, Rev. Mod. Phys. **79**, 175 (2007).
[24] H. Gretarsson, J. Sauceda, N. H. Sung, M. Höppner, M. Minola, B. J. Kim, B. Keimer, and M. Le Tacon, Phys. Rev. B **96**, 115138 (2017).
[25] A. Yamanaka, N. Asayama, M. Sasada, K. Inoue, M. Udagawa, S. Nishizaki, Y. Maeno, and T. Fujita, Phys. C **263**, 516 (1996).
[26] J.-C. Philippe, B. Baptiste, C. Sow, Y. Maeno, A. Forget, D. Colson, M. Cazayous, A. Sacuto, and Y. Gallais, Phys. Rev. B **103**, 235147 (2021).
[27] H. Gretarsson, N. H. Sung, J. Porras, J. Bertinshaw, C. Dietl, J. A. N. Bruin, A. F. Bangura, Y. K. Kim, R. Dinnebier, J. Kim, A. Al-Zein, M. Moretti Sala, M. Krisch, M. Le Tacon, B. Keimer, and B. J. Kim, Phys. Rev. Lett. **117**, 107001 (2016).
[28] P. Warzanowski, N. Borgwardt, K. Hopfer, J. Attig, T. C. Koethe, P. Becker, V. Tsurkan, A. Loidl, M. Hermanns, P. H. M. van Loosdrecht, and M. Grüninger, Phys. Rev. Research **2**, 042007(R) (2020).
[29] J.-H. Lee, Y. Choi, S.-H. Do, B. H. Kim, M.-J. Seong, and K.-Y. Choi, npj Quantum Mater. **6**, 43 (2021).
[30] J. P. Clancy, H. Gretarsson, M. H. Upton, J. Kim, G. Cao, and Y.-J. Kim, Phys. Rev. B **100**, 104414 (2019).
[31] A. Abragam and B. Bleaney, *Electron paramagnetic resonance of transition ions* (Clarendon Press, 1970).
[32] V. M. Katukuri, K. Roszeitis, V. Yushankhai, A. Mitrushchenkov, H. Stoll, M. van Veenendaal, P. Fulde,

J. van den Brink, and L. Hozoi, Inorg. Chem. **53**, 4833 (2014).

[33] P. A. Fleury and R. Loudon, Phys. Rev. **166**, 514 (1968).

[34] G. Khaliullin and S. Okamoto, Phys. Rev. B **68**, 205109 (2003).

[35] M. Subramanian, M. Crawford, R. Harlow, T. Ami, J. Fernandez-Baca, Z. Wang, and D. Johnston, Phys. C **235-240**, 743 (1994).

[36] M. Itoh, T. Shimura, Y. Inaguma, and Y. Morii, J. Solid State Chem. **118**, 206 (1995).

[37] L. J. Sandilands, W. Kyung, S. Y. Kim, J. Son, J. Kwon, T. D. Kang, Y. Yoshida, S. J. Moon, C. Kim, and T. W. Noh, Phys. Rev. Lett. **119**, 267402 (2017).

[38] I. Battisti, W. O. Tromp, S. Riccò, R. S. Perry, A. P. Mackenzie, A. Tamai, F. Baumberger, and M. P. Allan, npj Quantum Mater. **5**, 91 (2020).

[39] G. Blesio, S. Beck, A. Georges, and J. Mravlje, arXiv:2304.13563.

[40] M. Braden, G. André, S. Nakatsuji, and Y. Maeno, Phys. Rev. B **58**, 847 (1998).

[41] I. Nagai, N. Shirakawa, N. Umeyama, and S.-I. Ikeda, J. Phys. Soc. Jpn. **79**, 114719 (2010).

Supplemental Material for
Spin-orbit exciton in a correlated metal: Raman scattering study of Sr_2RhO_4

I. Additional experimental data

The single-crystal samples were prepared with the optical floating-zone technique, then annealed in oxygen and characterized with magnetization and resistivity measurements to ensure complete oxygen stoichiometry. The magnetization was measured in a MPMS SQUID VSM with applied field of 1 T perpendicular to the c-axis of the crystal. The measurement was performed upon warming up after zero-field cooling. The resistivity was measured with the standard 4-point probe technique in PPMS with contacts attached to the side faces of the crystal for in-plane ρ_{ab} measurements, and on the top and bottom faces for ρ_c measurements. The results are presented in Fig. S1. The crystal orientation was determined by x-ray Laue diffraction, and confirmed by the phonon spectra shown in Fig. S2.
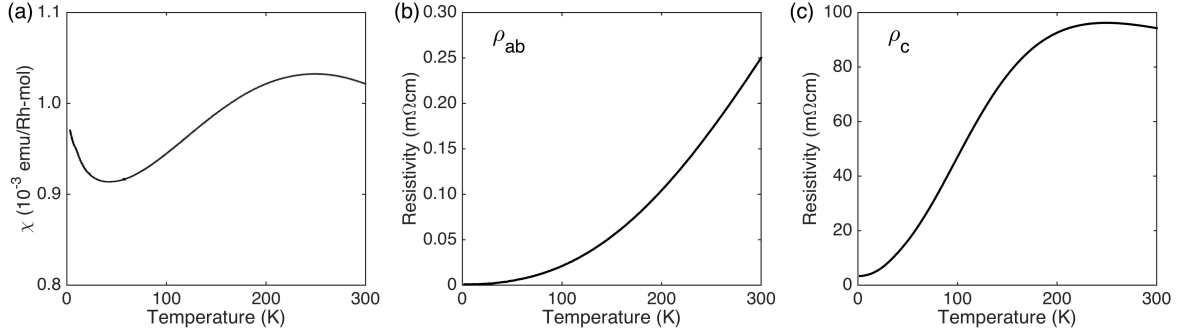

FIG. S1: Temperature dependence of (a) magnetization measured in a field of 1 T, and (b,c) in-plane ρ_{ab} and out-of-plane ρ_c resistivity. These results are consistent with those for full oxygen content samples [1].
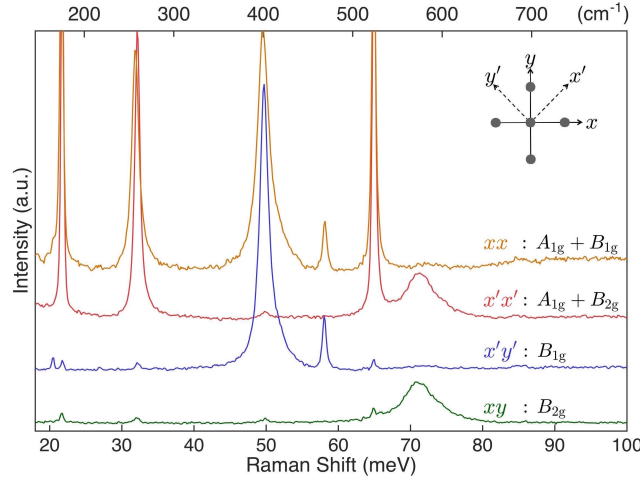

FIG. S2: Phonon spectra of Sr_2RhO_4 taken at 7 K. The data are vertically shifted for clarity.

During the Raman scattering measurements, the sample was mounted in a liquid-helium flow cryostat under ultra-high vacuum, and studied in a confocal backscattering geometry using a Jobin Yvon LabRAM HR800 spectrometer. The laser beam with a power of ~ 1 mW was focused to a ~ 10-μm-diameter spot on the freshly cleaved surface, and the scattered photons were resolved by a 600 grooves/mm grating. Two samples were measured, and they yielded the consistent results. Fig. S3 displays the temperature dependence of four polarization geometries. The spin-orbit exciton peaks persist in the xx, $x'x'$ and $x'y'$ channels from base to room temperature.

The pure A_{1g} signal was extracted from the raw data (after removing of the phonon peaks) in two different ways, as illustrated in Fig. S4. Both methods yield nearly identical spectra. Their average was taken as the resultant A_{1g} spectra and presented in Fig. 2 of the main text.
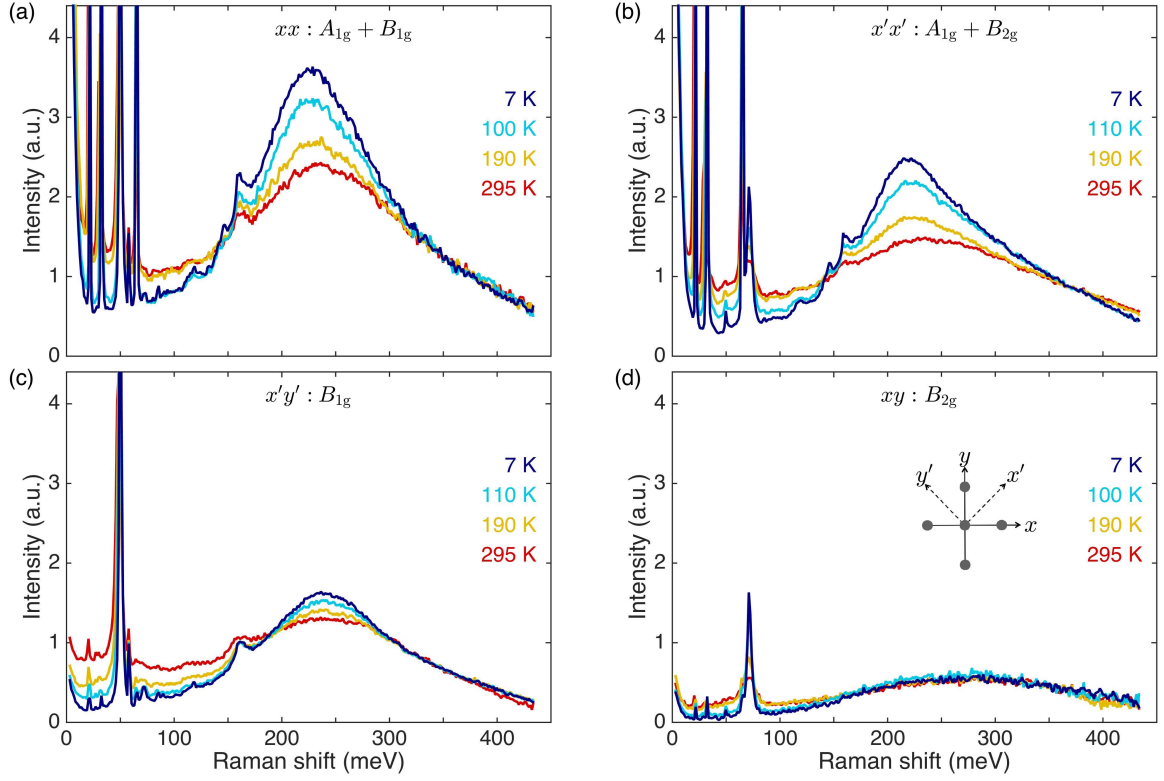
FIG. S3: Raman spectra taken at various temperatures in (a) xx, (b) $x'x'$, (c) $x'y'$, and (d) xy polarizations.
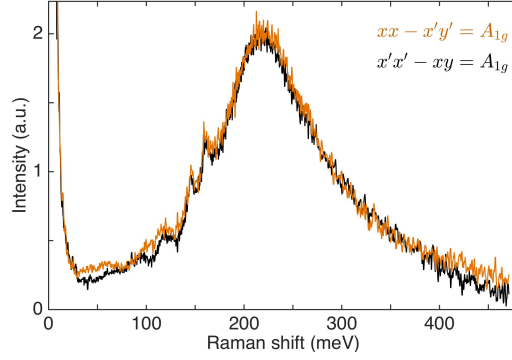

FIG. S4: The difference spectra between xx and $x'y'$ polarizations (black), and between $x'x'$ and xy polarizations (orange). Ideally, both should be identical to pure A_{1g} signal.

Most data were taken with the 632.8 nm (1.96 eV) excitation line from a He-Ne laser. To examine the influence of the incident photon energy, we also performed measurements with the 532 nm (2.33 eV) excitation line. As shown in Fig. S5, the higher-energy 532 nm excitation line induces additional intensity in both polarization channels, especially at higher energies above $\sim$300 meV, which is likely due to fluorescence. The spin-orbit exciton peaks, however, are robust and well defined independent on the incident photon energy. Relative positions of the peaks at different channels are also similar, i.e. the $x'x'$ channel peak is lower in energy than that of the $x'y'$ channel by about 20 meV.
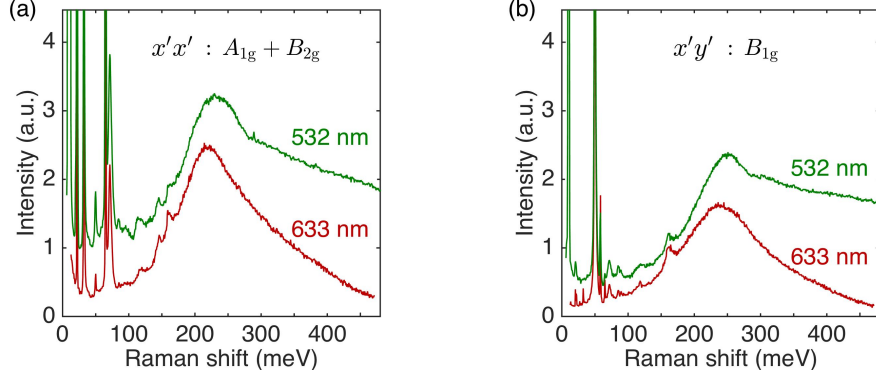
FIG. S5: Raman spectra taken at 7 K with different excitation lines.

II. Spin-orbital states of t_{2g}^5 electronic configuration in a tetragonal field

The energy levels and wavefunctions shown in Fig. 3(c) of the main text are derived from the single-ion Hamiltonian, comprising the spin-orbit coupling λ and tetragonal crystal field Δ terms:

$$\mathcal{H} = \lambda(\boldsymbol{l} \cdot \boldsymbol{s}) + \frac{\Delta}{3}(n_{yz} + n_{zx} - 2n_{xy}). \tag{S1}$$

We use here a hole representation, thus the positive Δ values stabilizing a planar xy orbital would correspond – within the point charge model – to the case of elongated octahedra. It should be noticed, however, that the point charge model is often insufficient, so the actual sign of Δ in a real material has to be determined experimentally. In terms of effective orbital angular momentum states $|l_z = 0\rangle = |xy\rangle$ and $|l_z = \pm 1\rangle = -\frac{1}{\sqrt{2}}(i|zx\rangle \pm |yz\rangle)$, the tetragonal field term reads as $\Delta(l_z^2 - \frac{2}{3})$. Diagonalization of this Hamiltonian results in three Kramers doublets: the ground state A with eigenvalue $\varepsilon_A = -\frac{1}{2}\varepsilon_B - \frac{1}{2}R$, and the higher energy states B and C with $\varepsilon_B = \frac{1}{2}\lambda + \frac{1}{3}\Delta$ and $\varepsilon_C = -\frac{1}{2}\varepsilon_B + \frac{1}{2}R$, respectively. Here, $R = \sqrt{\frac{9}{4}\lambda^2 + \Delta^2 - \lambda\Delta}$. The excitation energies corresponding to the $A \to B$ and $A \to C$ transitions then follow as:

$$E_{\mathrm{B}} = \varepsilon_B - \varepsilon_A = \frac{3}{4}\lambda + \frac{1}{2}\Delta + \frac{1}{2}R,$$
$$E_{\mathrm{C}} = \varepsilon_C - \varepsilon_A = R. \tag{S2}$$

At $\Delta = 0$, one has $R = \frac{3}{2}\lambda$, and thus $E_C = E_C = \frac{3}{2}\lambda$.

To calculate the spectral weights of spin-orbit excitons in the Raman spectra, we need to know the wavefunctions $|A\rangle$ etc. In the basis of $|l_z, s_z\rangle$ states, the ground state Kramers doublet functions read as:

$$|A_+\rangle = s_\theta \, |0, +\tfrac{1}{2}\rangle - c_\theta \, |+1, -\tfrac{1}{2}\rangle,$$
$$|A_-\rangle = s_\theta \, |0, -\tfrac{1}{2}\rangle - c_\theta \, |-1, +\tfrac{1}{2}\rangle. \tag{S3}$$

Here $c_\theta \equiv \cos\theta$, $s_\theta \equiv \sin\theta$, and angle $0 \leq \theta \leq \frac{\pi}{2}$ is given by $\tan 2\theta = 2\sqrt{2}\lambda/(\lambda - 2\Delta)$. In the cubic limit of $\Delta = 0$ with $s_\theta = \sqrt{\frac{1}{3}}$ and $c_\theta = \sqrt{\frac{2}{3}}$, Eq. S3 represents ideal total angular momentum $J = \frac{1}{2}$ states, equally contributed by all three t_{2g} orbitals. At large positive (negative) Δ values, the angle θ approaches 90° (0°), and the xy orbital contribution $\propto s_\theta$ to the ground state is enhanced (suppressed).

The B and C doublets correspond to the $J_z = \pm\frac{3}{2}$ and $J_z = \pm\frac{1}{2}$ states of $J = \frac{3}{2}$ quartet, correspondingly:

$$|B_+\rangle = |+1, +\tfrac{1}{2}\rangle, \qquad\qquad |C_+\rangle = c_\theta \, |0, +\tfrac{1}{2}\rangle + s_\theta \, |+1, -\tfrac{1}{2}\rangle,$$
$$|B_-\rangle = |-1, -\tfrac{1}{2}\rangle. \qquad\qquad |C_-\rangle = c_\theta \, |0, -\tfrac{1}{2}\rangle + s_\theta \, |-1, +\tfrac{1}{2}\rangle. \tag{S4}$$

III. Raman matrix elements and spin-orbit exciton intensities

In Eq. (2) of the main text, the Raman operator $\mathcal{R}_\gamma$ was presented in terms of spin $s = 1/2$ and orbital $l = 1$ angular momentum variables, as it follows from a general form of the spin-orbital exchange Hamiltonian. Now, we

represent this operator in the basis of spin-orbit entangled states given by Eqs. S3-S4 above. This results in a number of terms corresponding to Raman scattering from (**a**) low energy pseudospin fluctuations within the ground state A doublets (resulting in two-magnon scattering in insulators), (**b**) spin-orbit exciton transition $A \to B, C$ on one site of the exchange $\langle ij \rangle$ pair, and (**c**) spin-orbit excitons on both sites i and j. We note that spin-orbit exciton is created by intersite hopping between $J = 1/2$ and $J = 3/2$ states, see Fig. 4 in the main text. As this hopping is small in perovskites with 180° Me-O-Me bonding geometry, we keep only single-exciton terms. This gives, for the nearest-neighbor exchange bonds $\langle ij \rangle_x$ and $\langle ij \rangle_y$ along x and y directions of a square lattice, the following result:

$$\mathcal{R}_x = +\tfrac{1}{4}c_\theta \sum_{i,j_x} \left[c_\theta^2 (n_{BA} - s_\theta n_{CA})_i n_j - (1 + s_\theta^2)(\boldsymbol{\sigma}_{BA} - s_\theta \boldsymbol{\sigma}_{CA})_i \boldsymbol{\sigma}_j + 2s_\theta^2 (\sigma_{BA}^x)_i \sigma_j^x - 4\tau^2 s_\theta (n_{CA})_i \right] + H.c.,$$

$$\mathcal{R}_y = -\tfrac{1}{4}c_\theta \sum_{i,j_y} \left[c_\theta^2 (n_{BA} + s_\theta n_{CA})_i n_j - (1 + s_\theta^2)(\boldsymbol{\sigma}_{BA} + s_\theta \boldsymbol{\sigma}_{CA})_i \boldsymbol{\sigma}_j + 2s_\theta^2 (\sigma_{BA}^y)_i \sigma_j^y + 4\tau^2 s_\theta (n_{CA})_i \right] + H.c.. \quad \text{(S5)}$$

Here, $n = A_\sigma^\dagger A_\sigma$, $\sigma^x = A_{-\sigma}^\dagger A_\sigma$, $\sigma^y = i\sigma A_{-\sigma}^\dagger A_\sigma$, and $\sigma^z = \sigma A_\sigma^\dagger A_\sigma$ (sum over $\sigma = \pm 1$ is implied) are the density n and pseudospin $\boldsymbol{\sigma}$ operators acting within the ground state A doublet. While $n_{BA} = B_\sigma^\dagger A_\sigma$, $\sigma_{BA}^x = B_{-\sigma}^\dagger A_\sigma$, $\sigma_{BA}^y = i\sigma B_{-\sigma}^\dagger A_\sigma$, $\sigma_{BA}^z = \sigma B_\sigma^\dagger A_\sigma$, and similar operators $n_{CA} = C_\sigma^\dagger A_\sigma$ etc describe spin-orbit excitonic transitions from A level to the B and C levels, correspondingly. Excitons are created on site i, while a hole on nearest-neighbor sites $j = i \pm x$ or $j = i \pm y$ remains within the ground state A doublet.

The Raman operators of $\mathcal{R}_{A_{1g}}$ and $\mathcal{R}_{B_{1g}}$ are given by $\mathcal{R}_x \pm \mathcal{R}_y$. It is convenient to introduce the combinations $n_s^i = \tfrac{1}{4}(n_{i+x} + n_{i-x} + n_{i+y} + n_{i-y})$ and $n_d^i = \tfrac{1}{4}(n_{i+x} + n_{i-x} - n_{i+y} - n_{i-y})$ of A_{1g} and B_{1g} type symmetries, correspondingly. Then, the non-spin related part of the Raman operator can be written as

$$\mathcal{R}_{A_{1g}}^n = -c_\theta \sum_i \left[s_\theta (c_\theta^2 \, n_s + 4\tau^2 n_{CA} - c_\theta^2 \, n_d n_{BA}) \right]_i + H.c. , \qquad \mathcal{R}_{B_{1g}}^n = c_\theta^3 \sum_i \left[n_s n_{BA} - s_\theta \, n_d n_{CA} \right]_i + H.c. . \quad \text{(S6)}$$

Since B and C states have different J_z values, see Eq. (S4), the corresponding operators n_{BA} and n_{CA} transform under $\pi/2$ rotations about the z axis differently, i.e. with and without the sign change, respectively. This guarantees correct symmetry relations in the above equations (e.g., operator $n_d n_{BA}$ transforms as an object of A_{1g} symmetry).

Similarly, we introduce the A doublet pseudospin combinations $\boldsymbol{\sigma}_{s/d}^i = \tfrac{1}{2}(\boldsymbol{\sigma}_{i+x} + \boldsymbol{\sigma}_{i-x} \pm \boldsymbol{\sigma}_{i+y} \pm \boldsymbol{\sigma}_{i-y})$ near the central site i, and find the spin-related part of the Raman operator in the following form:

$$\mathcal{R}_{A_{1g}}^\sigma = \tfrac{1}{2}c_\theta \sum_i \left[s_\theta(1 + s_\theta^2) \, \boldsymbol{\sigma}_s \boldsymbol{\sigma}_{CA} - (1 + s_\theta^2) \, \sigma_d^z \sigma_{BA}^z - \sigma_d^x \sigma_{BA}^x - \sigma_d^y \sigma_{BA}^y + s_\theta^2 (\sigma_s^x \sigma_{BA}^x - \sigma_s^y \sigma_{BA}^y) \right]_i + H.c.,$$

$$\mathcal{R}_{B_{1g}}^\sigma = \tfrac{1}{2}c_\theta \sum_i \left[s_\theta(1 + s_\theta^2) \, \boldsymbol{\sigma}_d \boldsymbol{\sigma}_{CA} - (1 + s_\theta^2) \, \sigma_s^z \sigma_{BA}^z - \sigma_s^x \sigma_{BA}^x - \sigma_s^y \sigma_{BA}^y + s_\theta^2 (\sigma_d^x \sigma_{BA}^x - \sigma_d^y \sigma_{BA}^y) \right]_i + H.c.. \quad \text{(S7)}$$

Here, exciton creation on site i is accompanied by the A-doublet pseudospin dynamics on the nearest-neighbor sites.

Calculation of the Raman spectra lineshapes, which are determined by the correlation functions of the $\mathcal{R}^n$ and $\mathcal{R}^\sigma$ operators, is obviously a nontrivial task; it is, however, rather straightfoward to evaluate the spectral weights of the exciton transitions. In the density channel, we approximate the hole density n in the ground state A doublet as $\langle n \rangle \simeq 1$. This gives $n_s \simeq 1$ and $n_d \simeq 0$, and from Eq. (S6) we find the intensities of the $A \to B$ and $A \to C$ transitions:

	B exciton	C exciton
$I_{A_{1g}}^n :$	0	$s_\theta^2 c_\theta^2 (c_\theta^2 + 4\tau^2)^2$
$I_{B_{1g}}^n :$	c_θ^6	0 .

$$\text{(S8)}$$

We recall that $\tau = \tilde{t}/t = \sin 2\alpha \, (t_{pd\sigma}/t_{pd\pi})$, where $\tilde{t}$ is the hopping amplitude between t_{2g} and e_g orbitals, which is allowed due to in-plane rotations of the RhO$_6$ octahedra. In Sr$_2$RhO$_4$, the angle $\alpha = 10.5°$ [2] and $\sin 2\alpha = 0.36$.

For the transitions involving spin dynamics, we neglect non-local spin correlations (a reasonable approximation for paramagnetic Sr$_2$RhO$_4$), by setting $\langle \sigma_i^\alpha \sigma_j^\beta \rangle = \delta_{i,j}\delta_{\alpha,\beta}$. This gives $\langle \sigma_s^\alpha \sigma_s^\beta \rangle_i = \langle \sigma_d^\alpha \sigma_d^\beta \rangle_i = \delta_{\alpha,\beta}$, while $\langle \sigma_s^\alpha \sigma_d^\beta \rangle_i = 0$ by symmetry. As a result, we find

	B exciton	C exciton
$I_{A_{1g}}^\sigma = I_{B_{1g}}^\sigma :$	$\tfrac{1}{4}c_\theta^6 + \tfrac{1}{2}c_\theta^2(1 + s_\theta^2)^2$	$\tfrac{3}{4}c_\theta^2 s_\theta^2(1 + s_\theta^2)^2$.

$$\text{(S9)}$$

From Eqs. (S8) and (S9), the total intensities $I_{B/C} = (I^n + I^\sigma)_{B/C}$ in Eqs. (3) and (4) of the main text, follow.

Few comments on the above results are in order. First, both B and C excitons contribute to A_{1g} and B_{1g} spectra. Their relative spectral weights in the two channels are different, however, with the C and B contributions being more pronounced in A_{1g} and B_{1g} spectra, respectively. This allows one to determine the crystal field parameter Δ from the polarization dependence of the Raman spectra. As illustrated in Fig. S6, the A_{1g} and B_{1g} peaks switch their relative positions as Δ changes its sign, and the experimental data clearly rules out the negative Δ values in Sr_2RhO_4.
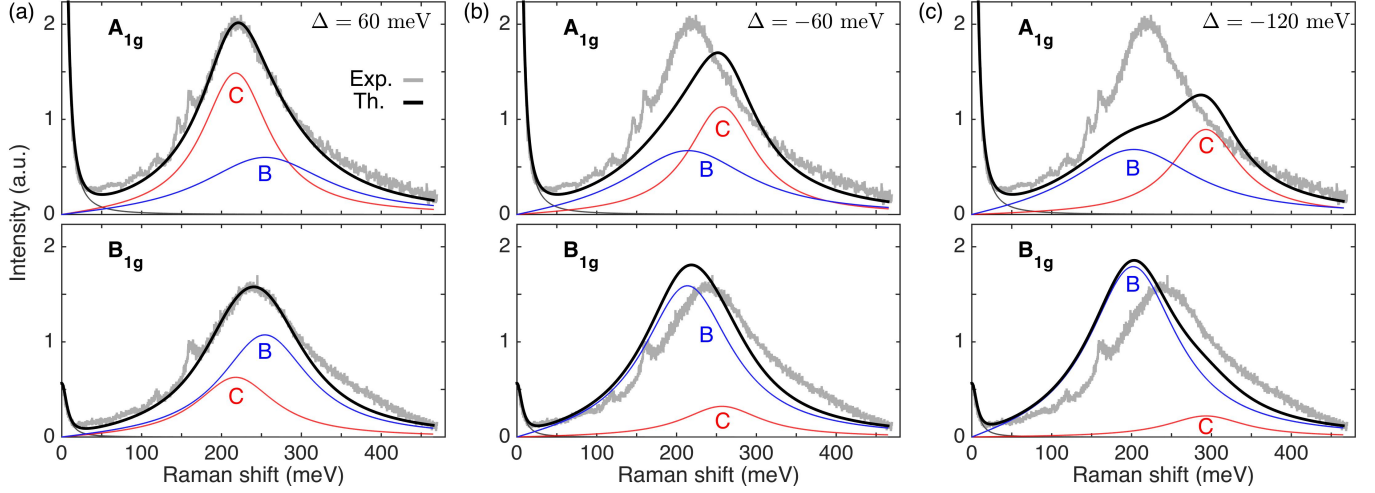

FIG. S6: Raman spectra calculated using different Δ values in Eq. (S1): (a) 60 meV, (b) -60 meV, and (c) -120 meV. Other parameters used are: λ=154 meV and $t_{pd\sigma}/t_{pd\pi} = 1.2$. The notations and experimental data are the same as in Fig. 2 of the main text.

Second, we note that calculations within the t_{2g} orbital space alone, i.e. without including $\tilde{t}$ hopping to the e_g states, give the A_{1g} intensity always smaller than that in B_{1g} channel, independent of Δ/λ ratio. In fact, as an attempt to remedy this discrepancy with experiment, we first inspected the Raman process within a single RhO_6 unit cell. Due to spin-orbit coupling, local $A \to B, C$ excitations are possible via $O(2p)$-$Rh(4d)$ dipolar transitions. Simple analysis of this scenario gives $I_{A_{1g}} \propto s_\theta^2 c_\theta^2$ and $I_{B_{1g}} \propto c_\theta^2$, i.e. exciton spectral weight in the A_{1g} channel would have been smaller by a factor of $s_\theta^2 \sim 1/3$, in sharp contrast to experimental result of $I_{A_{1g}} > I_{B_{1g}}$. This observation has prompted us to include the $\tilde{t}$-hopping processes, which are activated by the rotations of the RhO_6 octahedra. Note that these processes contribute only to the A_{1g} channel, see Eq. (S8). As a result, the A_{1g} intensity is enhanced and the A_{1g} vs B_{1g} intensity issue is resolved, as demonstrated in Fig. S7.
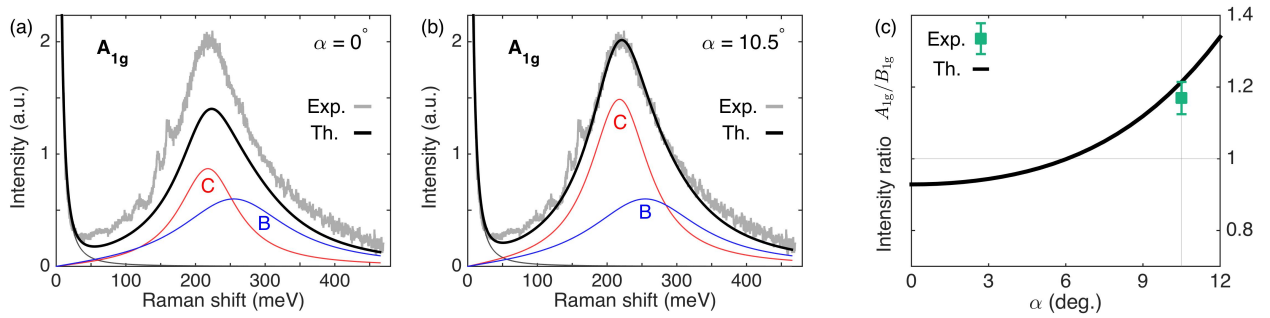

FIG. S7: The A_{1g} Raman spectra calculated using different octahedral rotation angles: (a) $\alpha = 0$, and (b) $\alpha = 10.5°$ as in Sr_2RhO_4 [2]. (c) Intensity ratio between A_{1g} and B_{1g} channels as a function of angle α. The experimental ratio is reproduced at a realistic value of $\alpha = 10.5°$. The parameters used are: λ=154 meV, Δ=60 meV, and $t_{pd\sigma}/t_{pd\pi} = 1.2$.

Finally, we note that the above theory – with modifications including magnetic order effects – is applicable to Sr_2IrO_4, which has a very similar lattice structure. The single-exciton peaks are observed in this material [3]. Importantly, the relative order of the A_{1g} and B_{1g} peak positions (A_{1g} is *higher* in energy than B_{1g}) is different from that in Sr_2RhO_4. We also note that, in contrast to perovskites, the intersite hopping between $J = 1/2$ and $J = 3/2$ states is not small in compounds with 90° Me-O-Me bonding geometry, making the double-exciton transitions equally

important for Raman scattering process. A nice example of this is the Kitaev material $RuCl_3$, where both single and double-exciton peaks have been clearly observed [4, 5].

———————————

* lichen.wang@fkf.mpg.de
† huimei.liu@ifw-dresden.de
‡ m.hepting@fkf.mpg.de
§ b.keimer@fkf.mpg.de

[1] I. Nagai, N. Shirakawa, N. Umeyama, and S.-I. Ikeda, J. Phys. Soc. Jpn. **79**, 114719 (2010).
[2] M. Subramanian, M. Crawford, R. Harlow, T. Ami, J. Fernandez-Baca, Z. Wang, and D. Johnston, Phys. C: Superconductivity **235-240**, 743 (1994).
[3] J.-A. Yang, Y.-P. Huang, M. Hermele, T. Qi, G. Cao, and D. Reznik, Phys. Rev. B **91**, 195140 (2015).
[4] P. Warzanowski, N. Borgwardt, K. Hopfer, J. Attig, T. C. Koethe, P. Becker, V. Tsurkan, A. Loidl, M. Hermanns, P. H. M. van Loosdrecht, and M. Grüninger, Phys. Rev. Research **2**, 042007(R) (2020).
[5] J.-H. Lee, Y. Choi, S.-H. Do, B. H. Kim, M.-J. Seong, and K.-Y. Choi, npj Quantum Mater. **6**, 43 (2021).